THE ASTROPHYSICAL JOURNAL SUPPLEMENT SERIES, 136:119–135, 2001 September

X-RAYS FROM SUPERBUBBLES IN THE LARGE MAGELLANIC CLOUD. VI. A SAMPLE OF THIRTEEN SUPERBUBBLES

BRYAN C. DUNNE, SEAN D. POINTS, AND YOU-HUA CHU
Department of Astronomy, University of Illinois, 1002 West Green Street, Urbana, IL 61801;
carolan@astro.uiuc.edu, points@astro.uiuc.edu, chu@astro.uiuc.edu
Received 2001 January 10; accepted 2001 March 12

ABSTRACT

We present *ROSAT* observations and analysis of thirteen superbubbles in the Large Magellanic Cloud. Eleven of these observations have not been previously reported. We have studied the X-ray morphology of the superbubbles and have extracted and analyzed their X-ray spectra. Diffuse X-ray emission is detected from each of these superbubbles, and X-ray emission is brighter than that theoretically expected for a wind-blown bubble, suggesting that the X-ray emission from the superbubbles has been enhanced by interactions between the superbubble shell and interior supernova remnants. We have also found significant positive correlations between the X-ray luminosity of a superbubble and its Hα luminosity, expansion velocity, and OB star count. Further, we have found that a large fraction of the superbubbles in the sample show evidence of breakout regions, where hot X-ray–emitting gas extends beyond the Hα shell.

Subject headings: galaxies: individual (Large Magellanic Cloud) — ISM: bubbles

1. INTRODUCTION

Superbubbles are large ($\sim$100 pc across) shells in the interstellar medium (ISM) created by the combined action of stellar winds and supernova explosions of massive stars in an OB association. The hot ($\gtrsim 10^6$ K) shock-heated gas interior to superbubbles emits X-ray radiation. X-ray observations of superbubbles can reveal a wealth of information on the structure and interior of superbubbles. An excess of diffuse X-ray emission in superbubbles can indicate the presence of interior supernova remnants (SNRs) shocking the inner walls of the superbubble shell (Chu & Mac Low 1990, hereafter Paper I; Wang & Helfand 1991). The diffuse X-ray emission can also be used to find breakout regions, where the hot gas from the superbubble interior may be leaking out into the ISM. Unresolved peaks superposed on the diffuse X-ray emission may also indicate the presence of stellar X-ray sources interior to the superbubble.

The Large Magellanic Cloud (LMC) provides an ideal laboratory for observing superbubbles in the X-ray spectrum. The coverage of Galactic superbubbles is far from complete because of extinction from the disk of the Milky Way. Non-Magellanic Cloud extragalactic superbubbles are too far away to be angularly resolved by X-ray instruments such as *ROSAT*. The LMC, however, provides a sample in excess of 20 superbubbles at a common distance ($\sim$50 kpc; Feast 1999) that are resolvable by modern X-ray detectors. Observations of the superbubbles in the LMC can provide us with great insight into the interaction among superbubbles, SNRs, and the ISM.

We have been studying X-ray emission from superbubbles in the LMC. In Paper I, *Einstein* observations were used to show that seven LMC superbubbles are diffuse X-ray sources with luminosities much higher than those expected by the wind-blown, pressure-driven bubble models of Weaver et al. (1977). Off-center SNRs are proposed to be responsible for the excess X-ray emission. *ROSAT* observations of the superbubble N44 confirmed its diffuse X-ray emission and provided the first useful X-ray spectra of N44 for determinations of plasma temperatures (Chu et al. 1993, hereafter Paper II). To illustrate that excess X-ray emission from superbubbles is caused by an intermittent process, Chu et al. (1995, hereafter Paper III) analyzed *ROSAT* observations of four X-ray–dim superbubbles and showed that these superbubbles do not have excess X-ray emission. For high-resolution spectral analysis, *ASCA* observations of N44 were made; the *ASCA* data showed that the hot gas in the breakout region is slightly cooler than that in the superbubble interior (Magnier et al. 1996, hereafter Paper IV). *ROSAT* observations of the H II complex N11 were analyzed to study the interaction between OB associations, H II regions, and superbubbles (Mac Low et al. 1998, hereafter Paper V).

In this latest study, we have analyzed *ROSAT* observations of eleven Hα-identified superbubbles in the LMC whose observations had not been reported previously. Diffuse X-ray emission was detected in every one of these eleven superbubbles. We have reanalyzed N44 and N11 to obtain a homogeneous set of results for comparisons. We have modeled these superbubbles using the pressure-driven bubble models of Weaver et al. (1977). In this paper, we report the *ROSAT* observations of the thirteen superbubbles studied and discuss the X-ray luminosities and other properties of the superbubbles and their relationship with the LMC.

2. X-RAY DATA SET AND ANALYSIS

2.1. *ROSAT Archival Data Set*

Our data set is based on a selection of known LMC superbubbles around OB associations with a well-defined Hα morphology. We have further constrained the sample to include only those superbubbles with previously unreported *ROSAT* observations with at least 5 ks exposure. The superbubbles studied are in N51, N57, N103, N105, N144, N154, N158, N160, N206 (nomenclature of Henize 1956), and 30 Dor C. Two superbubbles are present in N51, making the total number of superbubbles eleven. For comparisons with previous results, we have also included N11 and N44 in the data set. The coordinates, sizes, Hα lumi-

nosities, expansion velocities, and local OB associations of this sample of thirteen superbubbles, as well as alternative designations, are summarized in Table 1.

Two detectors are available on board the *ROSAT* satellite: the Position Sensitive Proportional Counter (PSPC) and the High Resolution Imager (HRI). We have used PSPC observations to investigate the physical conditions and distribution of the 10^6 K gas interior to most of the LMC superbubbles in our data set. The PSPC is sensitive to X-ray photons with energies in the range 0.1–2.4 keV and has an energy spectral resolution of $\sim 40\%$ at 1 keV, with a field of view of $\sim 2^\circ$. As the HRI is better suited to revealing point sources rather than diffuse emission, we have used HRI observations to investigate the distribution of X-ray–emitting gas only in the superbubble N206, which lies close to the outer edge of the field of view in the PSPC observations. The HRI is sensitive in the energy range 0.1–2.0 keV, with a field of view of $\sim 40'$. Further information on the PSPC and HRI can be found in Pfefferman et al. (1987) and the *ROSAT* Mission Description (1991). A summary of the individual observations can be found in Table 2.

2.2. *X-Ray Data Analysis*

We have studied both the X-ray morphology and X-ray spectra of the superbubbles in the data set. All the data were reduced using standard routines in IRAF[1] and the PROS package.[2]

2.2.1. *Morphology*

Analysis of the X-ray morphology of each superbubble was conducted using smoothed PSPC and HRI images. The images were binned to 4″ pixels and then smoothed with a Gaussian function of $\sigma = 4$ pixels. We have compared the X-ray morphologies with the Hα morphologies observed in the PDS scans of the Curtis Schmidt plates of Kennicutt & Hodge (1986). In Figure 1, we present the Hα images overlaid with X-ray contours. We also present the X-ray images overlaid with the same contours to ensure the clarity of the contour levels. The contours are at levels of 50%, 70%, 85%, and 95% of the peak level within the superbubble. For bright X-ray objects in the field not actually part of the superbubble (such as SNRs), we have plotted additional contours at 2, 4, 8, and 16 times the superbubble peak level. These contours are plotted as dashed lines.

2.2.2. *Spectral Fits*

The X-ray spectra of the superbubbles were extracted from the PSPC data. We defined source regions for each superbubble. Then, possible stellar sources (i.e., X-ray binaries and Wolf-Rayet stars) were excised from the data before the spectra were extracted. Additionally, we selected several background regions around each superbubble (this is especially important for superbubbles superposed on large extended LMC sources of diffuse X-ray emission, such as the 30 Doradus complex and the supergiant shells LMC 2 and LMC 3). The background-subtracted spectra were then extracted from the PSPC event files.

The observed X-ray spectrum of each superbubble is a convolution of several factors: the intrinsic X-ray spectrum of the superbubble, the intervening interstellar absorption, and the PSPC response function. Because the interstellar absorption and the PSPC response function depend on photon energy, we must assume models of the intrinsic X-ray spectrum and the interstellar absorption to make the problem tractable. As the X-ray emission from the superbubble interiors appears largely diffuse, we have used the Raymond & Smith (1977) thin-plasma emission model and the Morrison & McCammon (1983) effective absorption cross-section per hydrogen atom to describe the intrin-

[1] Image Analysis and Reduction Facility (IRAF) is distributed by the National Optical Astronomy Observatories, which are operated by the Association of Universities for Research in Astronomy, Inc., under cooperative agreement with the National Science Foundation.

[2] PROS/XRAY Data Analysis System; see http://hea-www.harvard.edu/PROS/pros.html.

TABLE 1

LMC Superbubble Properties

Object[a]	DEM[b]	Local OB Associations[c]	α (2000.0)	δ (2000.0)	Size[d] (pc × pc)	log $L_{H\alpha}$[d] (ergs s^{-1})	Expansion Velocity (km s^{-1})
N11 shell 1.....	DEM L 34	LH 9	04 56 51	−66 24 24	150 × 100	36.90	45[e]
N44	DEM L 152	LH 47	05 22 08	−67 56 12	100 × 75	37.00	40[f]
N51	DEM L 192	LH 51, LH 54	05 26 14	−67 30 18	135 × 120	37.04	20–50[g]
N51	DEM L 205	LH 63	05 28 06	−67 28 36	65 × 50	36.26	45–70[g]
N57	DEM L 229	LH 76	05 32 24	−67 41 18	135 × 105	36.91	∼45[g]
N103B.....	DEM L 84	NGC 1850	05 08 54	−68 45 00	120 × 120	36.53	20[h]
N105.....	DEM L 86	LH 31	05 09 57	−68 53 31	90 × 60	36.82	–
N144.....	DEM L 199	LH 58	05 26 33	−68 51 48	120 × 75	36.98	20–30[g]
N154.....	DEM L 246	LH 81, LH 87	05 35 57	−69 38 54	180 × 120	37.10	...
N158.....	DEM L 269	LH 101, LH 104	05 39 33	−69 25 48	120 × 100	36.80	∼45[g]
N160.....	DEM L 284	LH 103	05 40 12	−69 37 06	180 × 150	37.22	≲20[g]
N206.....	DEM L 221	LH 66, LH 69	05 29 36	−71 00 00	90 × 90	36.95	∼30[g]
30 Dor C.....	DEM L 263	LH 90	05 38 42	−69 06 03	100 × 90	36.94	∼45[g]

Note.—Units of right ascension are hours, minutes, and seconds, and units of declination are degrees, arcminutes, and arcseconds.

[a] Nomenclature of Henize 1956, except 30 Dor C.

[b] Nomenclature of Davies et al. 1976.

[c] Nomenclature of Lucke & Hodge 1970, except NGC 1850.

[d] Determined from PDS scans of Kennicutt & Hodge 1986, includes only Hα emission from the superbubble shell.

[e] Rosado et al. 1996.

[f] Meaburn & Laspias 1991.

[g] Y.-H. Chu et al. 2001, in preparation.

[h] Georgelin et al. 1983.

TABLE 2

ARCHIVAL *ROSAT* OBSERVATIONS

Field, *ROSAT* ID	Principal Investigator	α (2000.0)	δ (2000.0)	Exposure Time (s)	Off-Axis Angle (arcmin)
N11:					
rp900320a01.....	Chu	04 56 33.6	−66 28 48	13731	4.7
rp900320n00.....	Chu	04 56 33.6	−66 28 48	17589	4.7
N44:					
rp400154n00.....	Pakull	05 22 26.4	−67 58 12	6522	2.2
rp500093n00.....	Chu	05 22 02.4	−67 55 12	8720	2.2
N51, N57:					
rp500054a00.....	Fink	05 25 52.8	−67 30 00	3420	5.3, 39.7
rp500054a01.....	Fink	05 25 52.8	−67 30 00	4452	5.3, 39.7
N103, N105:					
rp500037n00.....	Aschenbach	05 08 60.0	−68 43 48	6826	1.3, 11.0
N144:					
rp500138a01.....	Mac Low	05 26 36.0	−68 50 24	14531	1.4
rp500138a02.....	Mac Low	05 26 36.0	−68 50 24	14581	1.4
rp500138n00.....	Mac Low	05 26 36.0	−68 50 24	2478	1.4
N154, 30 Dor C:					
rp180251n00.....	Aschenbach	05 35 28.8	−69 16 12	20153	22.8, 13.4
rp500100a00.....	Gorenstein	05 35 28.8	−69 16 12	16957	22.8, 13.4
rp500100a01.....	Gorenstein	05 35 28.8	−69 16 12	9657	22.8, 13.4
rp500140a02.....	Gorenstein	05 35 28.8	−69 16 12	10758	22.8, 13.4
rp500140n00.....	Gorenstein	05 35 28.8	−69 16 12	2642	22.8, 13.4
rp500303n00.....	Hasinger	05 35 28.8	−69 16 12	9416	22.8, 13.4
N158:					
rp400052n00.....	Oegelman	05 40 12.0	−69 19 48	8823	10.9
rp400133n00.....	Oegelman	05 40 12.0	−69 19 48	1803	10.9
N160:					
rp400079n00.....	Lewin	05 39 38.4	−69 44 24	7429	7.9
N206:					
rp300172a01.....	Oegelman	05 32 28.8	−70 21 36	2993	41.0
rp300172a02.....	Oegelman	05 32 28.8	−70 21 36	3880	41.0
rp300172n00.....	Oegelman	05 32 28.8	−70 21 36	6272	41.0
rh600781a01.....	Chu	05 30 45.6	−71 02 24	24041	6.1
rh600781n00.....	Chu	05 30 45.6	−71 02 24	25238	6.1

sic X-ray spectra of the superbubbles and the foreground absorption, respectively. We then simulate the observed spectrum, combining the assumed models for the intrinsic spectrum and the interstellar absorption with the response function of the PSPC. The observed spectrum is fitted with the simulated spectra; the χ^2 of the fits determines the best fit.

We performed a χ^2 grid search of simulated spectral fits to determine the best-fit levels for the temperature, kT, and absorption column density, $N_{\rm H}$. From these model fits, we can calculate the unabsorbed X-ray flux and therefore the X-ray luminosity, $L_{\rm X}$, of the diffuse X-ray emission from the superbubbles. The normalization factor of the best fit can be used to determine the volume emission measure, adopting a distance of 50 kpc for the LMC (Feast 1999). If we assume a uniform density in the X-ray–emitting gas, the volume emission measure can be expressed as $N_e^2 f V$, where N_e is the electron density, f is the volume-filling factor, and V is the volume of the superbubble interior. Assuming the superbubbles have an ellipsoidal shape, we can use the observed diameters of the superbubbles to determine $N_e\sqrt{f}$. The net exposure time, background-subtracted source counts, scaled background counts, and best-fit values of kT, $N_{\rm H}$, $L_{\rm X}$, and $N_e\sqrt{f}$ for a 30% solar abundance Raymond & Smith (1977) thermal plasma model are given in Table 3. Plots of the fits to the superbubbles' X-ray spectra are shown in Figure 2.

We have also sought to constrain the models further by using observations of the H I column density to determine independently the total absorption column density, $N_{\rm H}$. We have divided the absorption column into Galactic and LMC components and determined each separately. Arabadjis & Bregman (1999) demonstrated that in the X-ray spectrum at Galactic latitudes $|b| > 25°$ the contribution of molecular gas to the total absorption column density is comparable to the contribution of the neutral hydrogen gas. We have therefore approximated the Galactic absorption column density by $N_{\rm H} \simeq 2 \times N_{\rm H\,I}$. Continuing this approximation to the LMC absorption column density is more complicated. Measurements of LMC H I column density can sample material both in front of and behind a feature such as a superbubble. We have used the simplifying assumption that half the LMC H I gas is foreground to the superbubbles and half is background. Thus, the LMC component of the total absorption column density is $\frac{1}{2} \times 2N_{\rm H\,I} = N_{\rm H\,I}$. The total absorption column density is therefore given by $N_{\rm H} = 2 \times (N_{\rm H\,I})_{\rm Galactic} + (N_{\rm H\,I})_{\rm LMC}$.

We have used the observations of Galactic and LMC H I column densities by Dickey & Lockman (1990) and Rohlfs et al. (1984) to determine the total absorption column density. These calculated values of $N_{\rm H}$ are, on average, nearly an order of magnitude larger than values of $N_{\rm H}$ determined by the best-fit models to the X-ray spectra (see Table 4). Indeed, several of the Galactic $N_{\rm H}$ values alone are

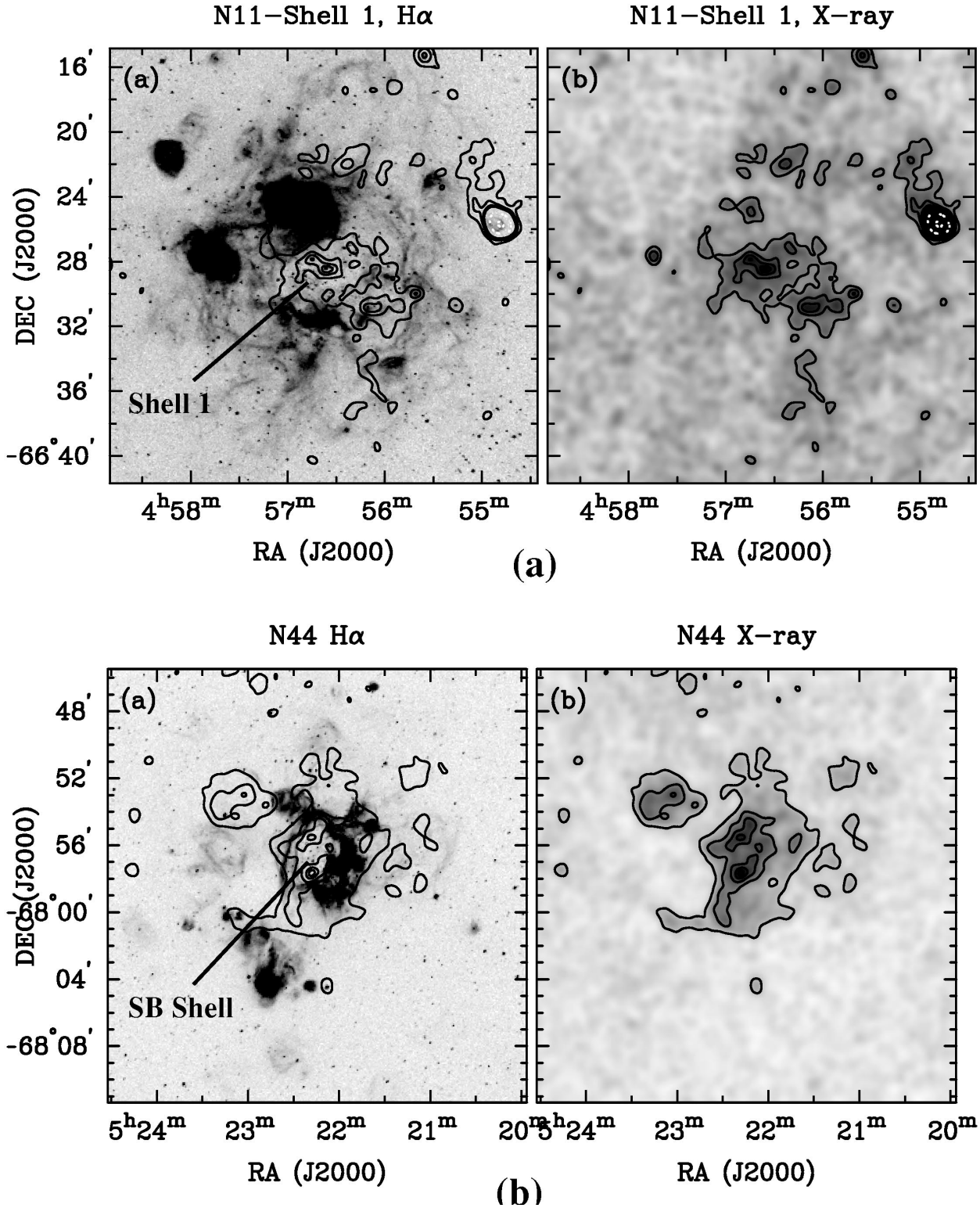

FIG. 1.— (*a*) N11 shell 1, (*b*) N44, (*c*) N51, (*d*) N57, (*e*) N103, (*f*) N105, (*g*) N144, (*h*) N154, (*i*) N158, (*j*) N160, (*k*) N206, and (*l*) 30 Dor C, showing Hα emission from the superbubble(s) overlaid with X-ray contours (*left*) and the X-ray emission overlaid with the same contours to ensure the clarity of the contour levels (*right*). The contours are at levels of 50%, 70%, 85%, and 95% of the peak level within the superbubble. For bright X-ray objects in the field not actually part of the superbubble (such as SNRs), we have plotted additional contours at 2, 4, 8, and 16 times the superbubble peak level (*dashed lines*). Locations of the superbubbles are indicated in the Hα images.

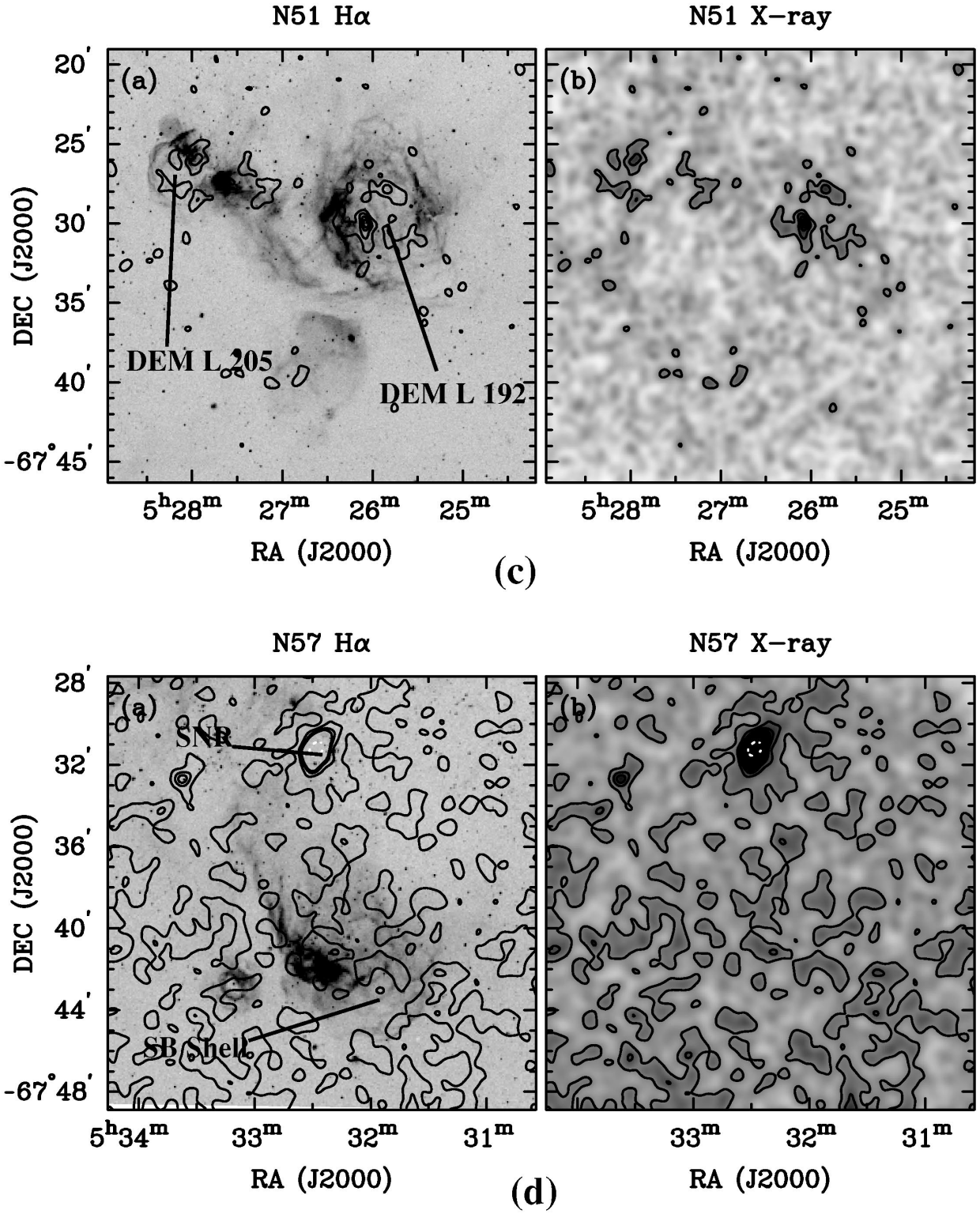

FIG. 1.—*Continued*

larger than those derived from the best-fit models. The calculated values of N_H also show a much narrower range of absorption column densities to the LMC superbubbles (log N_H = 21.3–21.7) than that of the values of N_H derived from the best-fit models to the X-ray spectra (log N_H = 20.4–22.0).

We have redetermined best-fit values for kT, L_X, and N_e, based again on a 30% solar abundance Raymond & Smith (1977) thermal plasma model, but with N_H fixed at the calculated values determined above. A summary of the results is given in Table 4. Plots of these fixed N_H fits to the superbubbles' X-ray spectra are shown in Figure 3.

3. INDIVIDUAL SUPERBUBBLE PROPERTIES

We will now discuss each of the superbubbles studied individually. For each superbubble, although we primarily

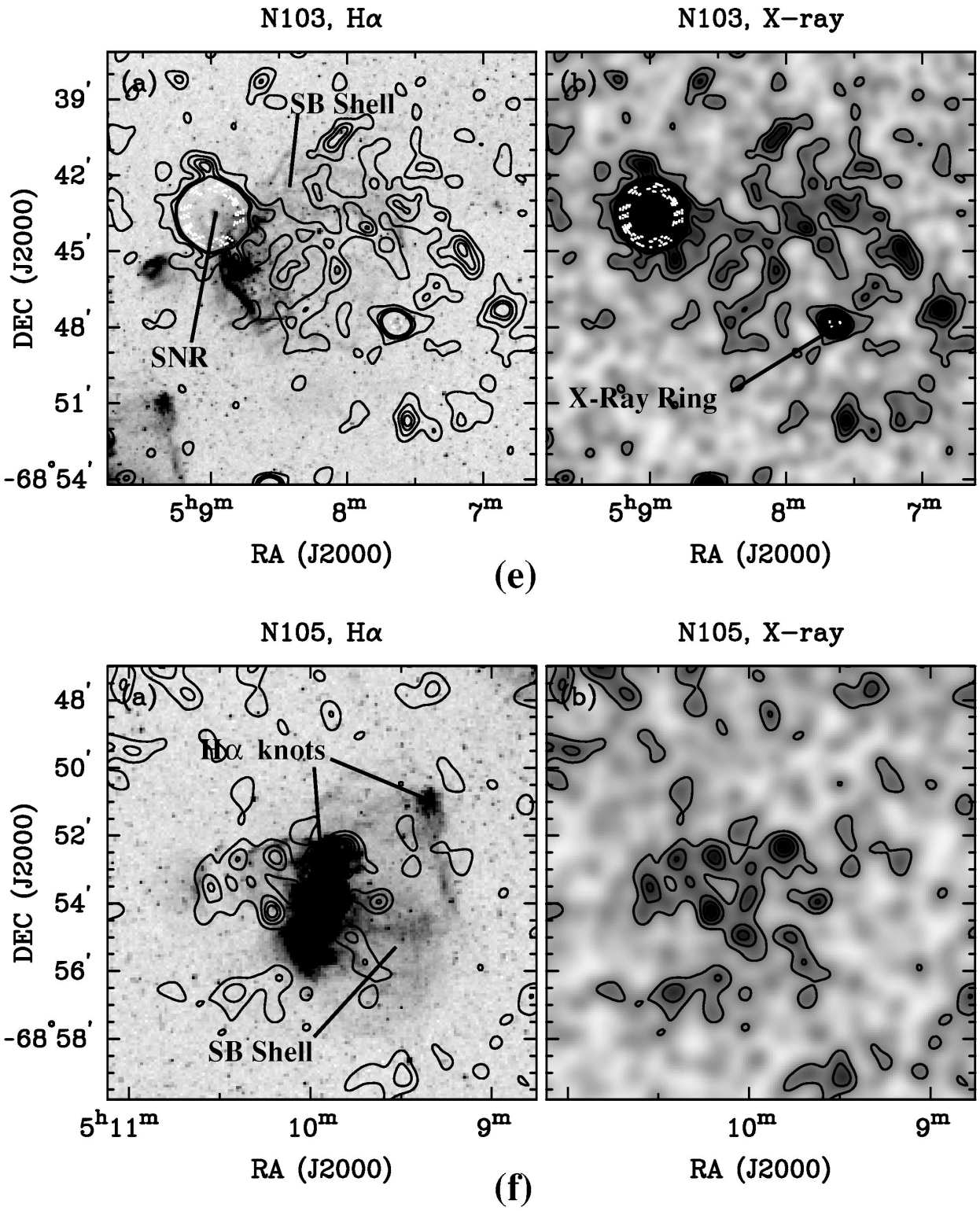

FIG. 1.—*Continued*

use the nomenclature of Henize (1956), e.g., N11, we give alternative designations as cataloged by Davies, Elliott, & Meaburn (1976), e.g., DEM L 192. We also give the OB associations and star clusters encompassed by the superbubble as reported in Lucke & Hodge (1970), e.g., LH 63. General descriptions of the Hα morphology, as seen in the PDS scans of the Curtis Schmidt plates of Kennicutt & Hodge (1986), and comparisons with X-ray morphology from the smoothed PSPC images are given. We also discuss breakout regions, possible identifications of X-ray hot spots with known stellar sources from Breysacher (1981), e.g., Br 81, and Sanduleak (1969), e.g., Sk −66°28, and other interesting X-ray features. The linear sizes of the superbubbles are calculated assuming $1' = 15$ pc.

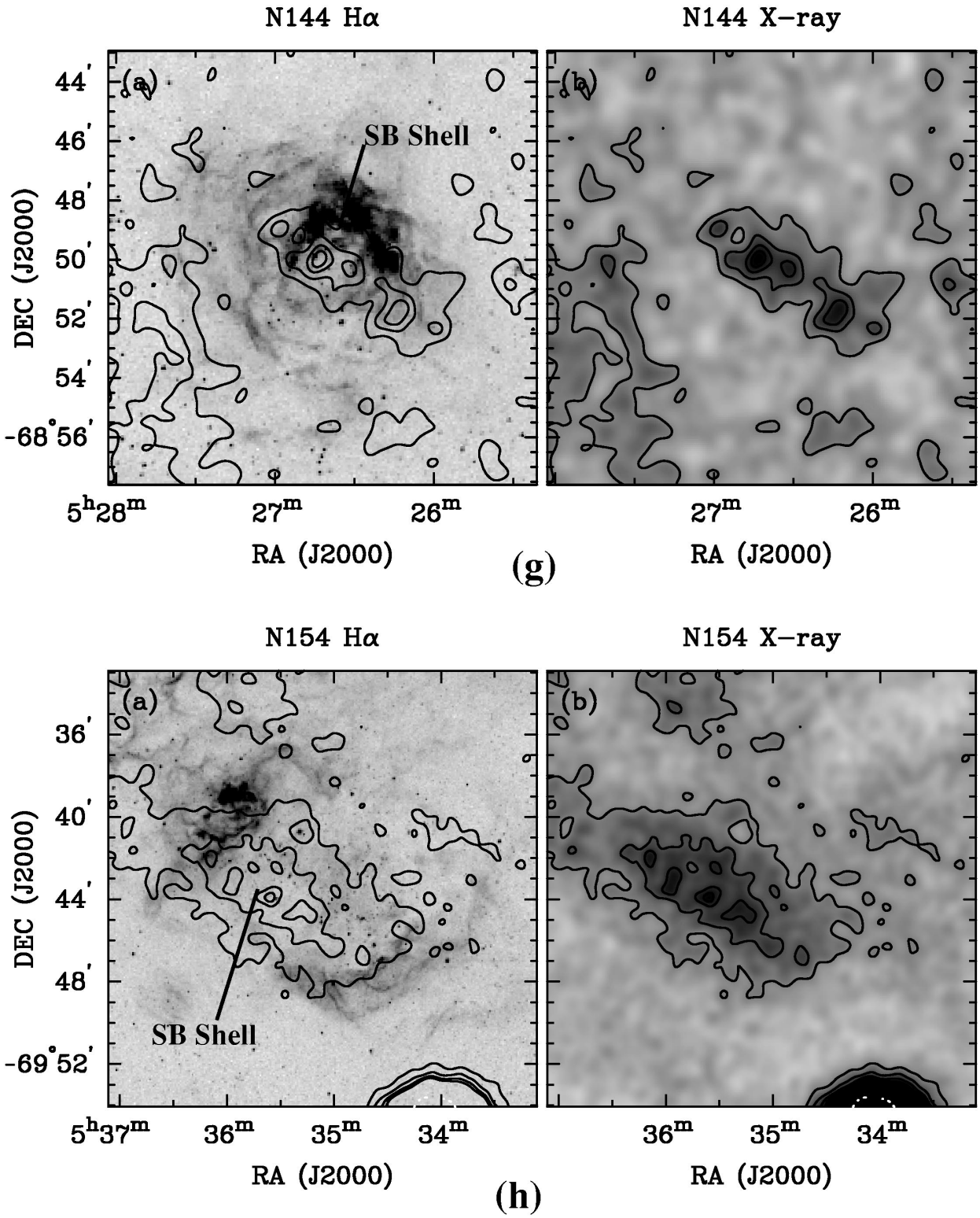

FIG. 1.—*Continued*

3.1. *N11 Shell 1*

N11 (DEM L 34) is the second-largest H II complex in the LMC (Kennicutt & Hodge 1986). N11 contains a superbubble 150 pc × 100 pc in size, surrounded by several bright Hα knots and smaller Hα shells. The superbubble has been labeled shell 1 in Paper V. Shell 1 encompasses the OB association LH 9. Diffuse X-ray emission is detected toward shell 1 (see Fig. 1*a*).

This diffuse X-ray emission is centrally bright and appears to be confined by the observed Hα shell. The X-ray emission peaks at a location coincident with HD 32228, a known Wolf-Rayet star also cataloged as Br 81 and Sk

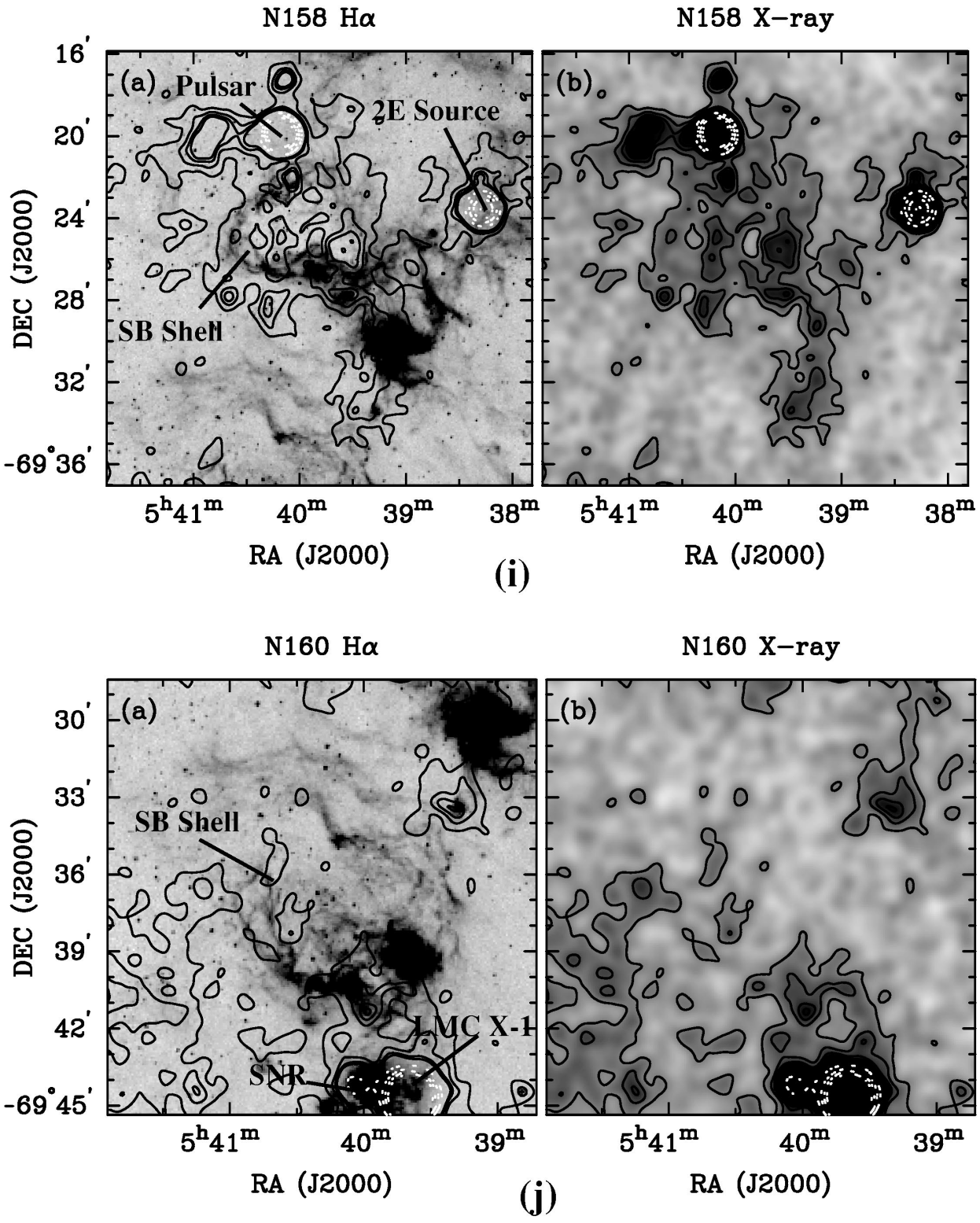

FIG. 1.—*Continued*

−66°28. Several smaller peaks are also evident in the diffuse X-ray emission. A more thorough interpretation of the X-ray emission can be found in Paper V.

3.2. *N44 (DEM L 152)*

N44 is a bright H II complex, similar to N11. N44 contains a superbubble, cataloged as DEM L 152, around the OB association LH 47. The 100 pc × 75 pc superbubble is well detected in Hα emission with well-defined shell walls. Diffuse X-ray emission is detected toward DEM L 152 (see Fig. 1*b*). Additionally, diffuse X-ray emission is detected ∼6′ to the northeast of DEM L 152; this emission has been identified in Paper II as originating from a supernova remnant.

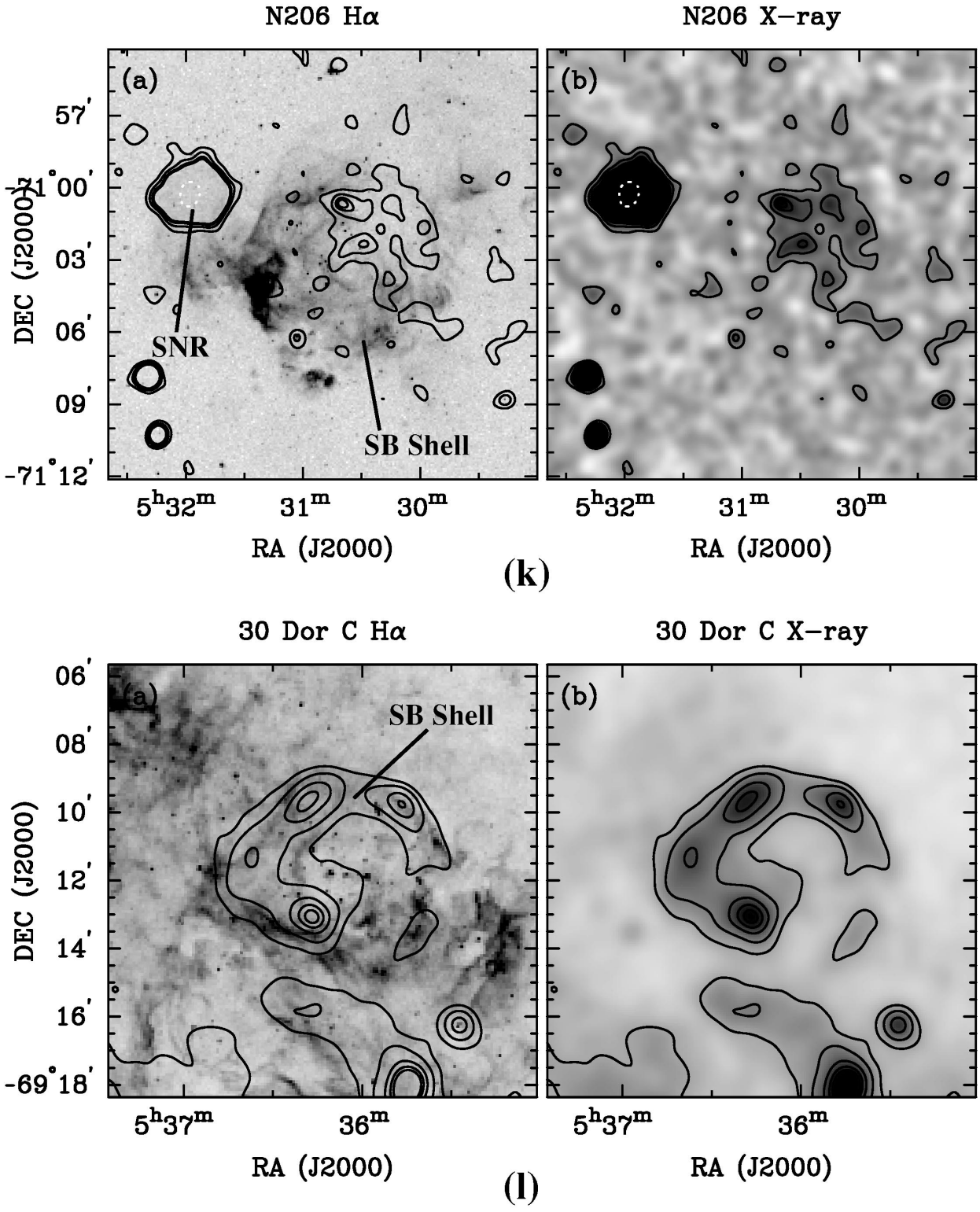

FIG. 1.—*Continued*

The diffuse X-ray emission correlates well with the Hα shell of DEM L 152. The X-ray emission is limb-brightened, forming an X-ray shell just interior to the Hα shell. A breakout region on the southern edge of the superbubble and an X-ray blister on the eastern edge of the shell are detected in the PSPC image as well. A more thorough interpretation of the X-ray emission and the breakout regions can be found in Papers II and IV.

3.3. *N51 (DEM L 192, DEM L 205)*

N51 is a nebular complex encompassing five OB associations, LH 51, 54, 55, 60, and 63 (Paper I). Two ionized gas shells are visible in the Hα image (see Fig. 1*c*) and are cataloged as DEM L 192 and DEM L 205. DEM L 192 is the larger shell, with size 135 pc × 120 pc, and it contains the OB associations LH 51 and LH 54. DEM L 205 is the

TABLE 3

BEST-FIT N_H LMC SUPERBUBBLE X-RAY SPECTRAL FITS

Object	Exposure (s)	Background-Subtracted Source Counts	Scaled Background Counts	log N_H (cm^{-2})	kT (keV)	log L_X[a] (ergs s^{-1})	$N_e\sqrt{f}$ (10^{-2} cm^{-3})
N11 shell 1	31320	1775	1667	21.9	0.13	37.17	31.
N44	15242	2894	1260	20.6	0.71	35.73	3.8
N51 DEM L 192.....	7872	559	865	20.4	0.28	35.18	1.5
N51 DEM L 205.....	7872	220	226	20.5	0.25	34.86	3.7
N57	7872	398	489	20.6	0.33	35.32	1.8
N103B.....	6826	99	120	21.3	0.72	34.85	0.8
N105	6826	158	183	21.6	0.31	35.40	4.6
N144	31590	667	1399	20.5	0.32	34.74	1.3
N154	81210	6269	9618	20.7	0.29	35.52	1.8
N158	10626	2543	1236	20.7	0.60	35.85	3.0
N160	7429	964	1517	20.9	3.40	35.80	1.9
N206	13145	330	490	20.7	0.31	35.09	2.2
30 Dor C East.....	81210	5378	4388	21.1	1.19	35.49	4.0
30 Dor C est	81210	1887	3225	22.0	1.22	35.84	7.4

[a] In the energy band 0.5–2.4 keV.

smaller shell, with size 65 pc × 50 pc. The morphology of DEM L 205 is that of a blister with the OB association LH 63 at the base. Diffuse X-ray emission is detected toward both of these optical shells.

The diffuse X-ray emission toward DEM L 192 is limb-brightened and confined within the optical Hα shell. Therefore, it is reasonable to conclude that the X-ray emission is produced by hot gas interior to the superbubble. Additionally, an X-ray hot spot is detected within the superbubble and coincides with the Wolf-Rayet star Br 31, also cataloged as Sk −67°104. Emission from this hot spot was excluded in the thermal plasma model fit of DEM L 192.

It is not clear whether the X-ray hot spot is a peak in the diffuse emission or a stellar source. Only 42 ± 11 PSPC counts were detected from the hot spot. This count level is inadequate to constrain the three parameters on which a thermal plasma emission model depends. Further high-resolution X-ray observations are needed to explore the nature of this hot spot.

DEM L 205 also shows limb brightening in the PSPC images. Unlike DEM L 192, no X-ray hot spots are detected within DEM L 205. On the southwestern side of this shell, where the Hα surface brightness is lowest, the X-ray emission appears more extended than the main shell. X-ray emission of similar morphology is also detected in the *Einstein* observations of N51 (Paper I). This may indicate a breakout of the hot gas interior to DEM L 205 into a lower density region; however, the Hα image hints at the presence of very faint outer Hα filaments confining this emission.

3.4. *N57 (DEM L 229)*

N57 is a nebular complex encompassing the OB associ-

TABLE 4

FIXED N_H LMC SUPERBUBBLE X-RAY SPECTRAL FITS

Object	log $(N_{H\,I})_{Galactic}$[a] (cm^{-2})	log $(N_{H\,I})_{LMC}$[b] (cm^{-2})	log N_H (cm^{-2})	kT (keV)	log L_X[c] (ergs s^{-1})	$N_e\sqrt{f}$ (10^{-2} cm^{-3})
N11 shell 1	20.63	21.45	21.6	0.24	35.96	4.2
N44	20.79	21.45	21.6	0.35	36.36	9.3
N51 DEM L 192.....	20.78	21.07	21.4	0.18	35.82	4.1
N51 DEM L 205.....	20.77	20.89	21.3	0.18	35.37	8.2
N57	20.78	21.23	21.5	0.23	35.91	4.3
N103B.....	20.79	21.30	21.5	0.65	35.02	1.0
N105	20.81	21.30	21.5	0.34	35.28	3.5
N144	20.79	20.87	21.3	0.25	35.12	2.3
N154	20.82	21.58	21.7	0.15	36.88	14.
N158	20.83	21.52	21.7	0.28	36.66	10.
N160	20.84	21.53	21.7	0.93	36.07	2.4
N206	20.84	21.27	21.5	0.20	35.80	6.1
30 Dor C East.....	20.81	21.63	21.7	0.79	35.90	5.4
30 Dor C West.....	20.81	21.63	21.7	[d]	35.54	5.1

[a] Dickey & Lockman 1990.
[b] Rohlfs et al. 1984.
[c] In the energy band 0.5–2.4 keV.
[d] Unable to find solution.

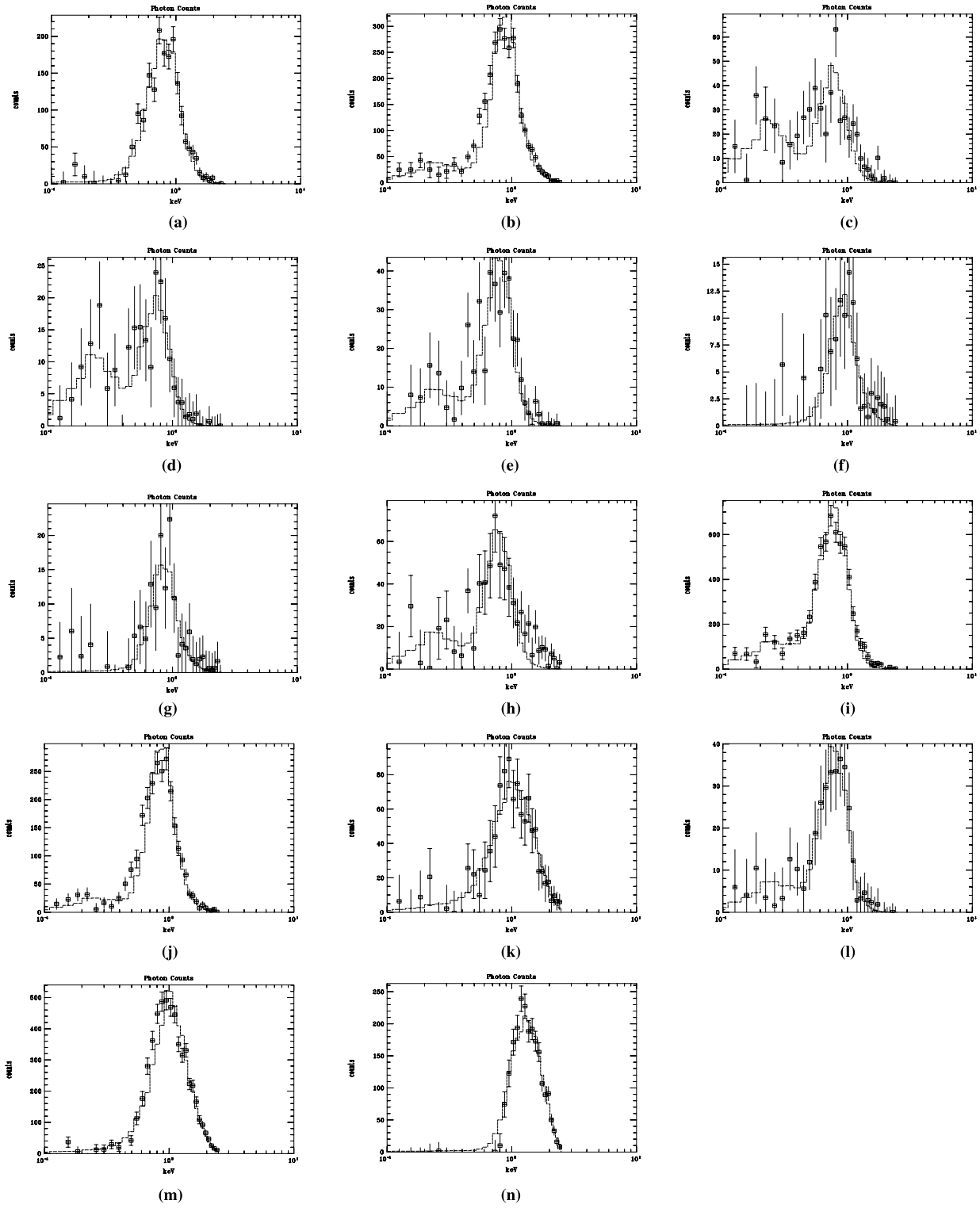

FIG. 2.—X-ray spectra and the best-fit N_H spectral fit for the superbubbles (*a*) N11 shell 1, (*b*) N44, (*c*) N51–DEM L 192, (*d*) N51–DEM L 205, (*e*) N57, (*f*) N103, (*g*) N105, (*h*) N144, (*i*) N154, (*j*) N158, (*k*) N160, (*l*) N206, (*m*) 30 Dor C east side, and (*n*) 30 Dor C west side.

ation LH 76. Two ionized gas shells are visible in the Hα image (see Fig. 1*d*) and are cataloged as DEM L 229 and DEM L 231. DEM L 229 is the larger shell; it is 200 pc × 100 pc in size and contains LH 76. The smaller shell, DEM L 231, which is 30 pc × 30 pc, is a ring nebula around the Wolf-Rayet star Br 48 (Chu & Lasker 1980; Chu, Weis, & Garnett 1999). Of these two shells, diffuse X-ray emission is detected only toward DEM L 229. Additionally, a bright X-ray source is visible to the north of DEM L 229; the X-ray source is not associated with DEM L 229 and has been identified as the SNR candidate SNR 0532−675 (Mathewson et al. 1985; Williams et al. 1999).

The diffuse X-ray emission toward DEM L 229 coincides with the interior of the superbubble. The emission also

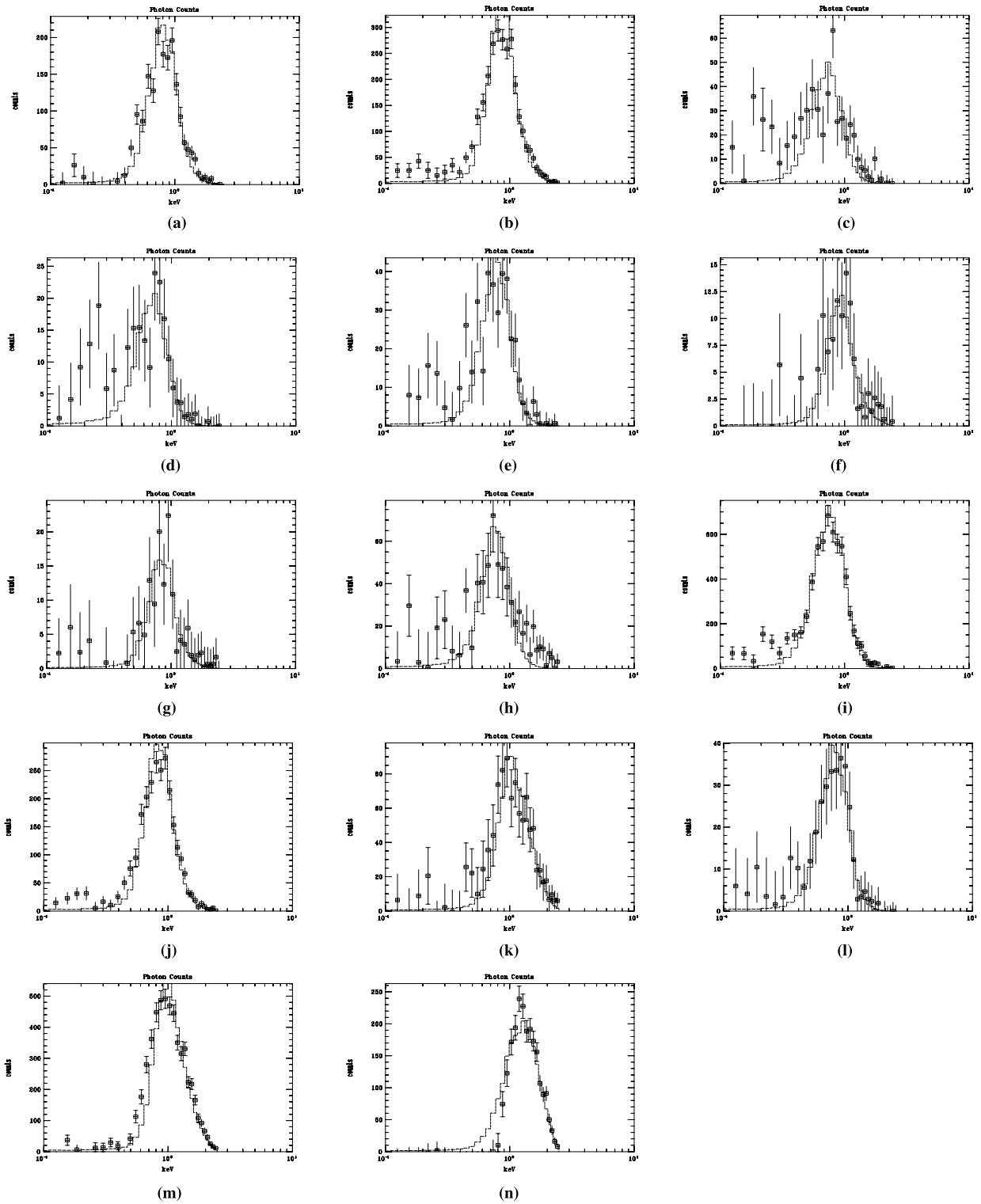

FIG. 3.—X-ray spectra and the fixed N_H spectral fit for the superbubbles (*a*) N11 shell 1, (*b*) N44, (*c*) N51–DEM L 192, (*d*) N51–DEM L 205. (*e*) N57, (*f*) N103, (*g*) N105, (*h*) N144, (*i*) N154, (*j*) N158, (*k*) N160, (*l*) N206, (*m*) 30 Dor C east side, and (*n*) 30 Dor C west side.

appears to be largely confined by the optical Hα shell. This indicates that the X-ray emission originates from the hot gas in the superbubble interior. The X-ray emission appears brightest toward the southern part of DEM L 229. Details of the X-ray morphology cannot be confidently determined, however, as N57 is detected on the outer edge of the PSPC (see Table 2) where the point-spread function becomes quite poor.

3.5. *N103 (DEM L 84)*

N103 is a nebular complex encompassing the star cluster NGC 1850. It has two main components, N103A (DEM L

85), the 20 pc × 15 pc Hα knot on the east, and N103B (DEM L 84), a 120 pc × 120 pc superbubble on the west.[3] Supernova remnant 0509−68.7 is present just exterior to the eastern edge of the superbubble (Mathewson et al. 1983; Williams et al. 1999), and the superbubble is brightest in Hα on the eastern side closest to the SNR. Diffuse X-ray emission is detected toward both the superbubble and the supernova remnant (see Fig. 1*e*).

The X-ray emission toward N103B appears to have several distinct structures. The most obvious is the very strong extended source coincident with the supernova remnant 0509−68.7. Another prominent structure is a large limb-brightened X-ray ring with a point X-ray source at the center. Chu et al. (2000) found that this X-ray ring is centered on the nearby star cluster HS122 (Hodge & Sexton 1966), which is projected at the southwest rim of the superbubble. We therefore cannot assume that the majority of the diffuse X-ray emission detected toward N103B is caused by hot gas inside the superbubble of N103B. Further comparison of the X-ray and Hα images presented in Figure 1*e* reveal diffuse X-ray emission in the region between the supernova remnant of N103B and the X-ray ring and coincident with the superbubble. Because of the low scattering levels of the PSPC, it is reasonable to assume that this X-ray emission arises from hot gas within the superbubble. We have used this region as a sample of the X-ray emission from the superbubble of N103B.

3.6. *N105* (*DEM L 86*)

N105 is a nebular region encompassing the OB association LH 31 (also cataloged as NGC 1858) and the star cluster NGC 1854. Two bright Hα knots are visible, as well as Hα emission from the filaments of the 90 pc × 60 pc superbubble shell. The larger Hα knot coincides with LH 31; the smaller knot coincides with NGC 1854. Diffuse X-ray emission is detected toward the larger Hα knot (see Fig. 1*f*).

The strongest X-ray emission from N105 coincides with LH 31, indicating that the X-ray emission is likely emitted by hot gas produced by the OB association. The diffuse X-ray emission is not confined by the Hα emission of N105; instead, the emission extends eastward from N105 to a nearby patch of Hα emission, DEM L 87. The diffuse X-ray emission appears to lose intensity approximately at the edge of DEM L 87. This suggests that the hot X-ray–emitting gas created by LH 31 is expanding eastward through a lower density medium to the denser gas in DEM L 87. At the interface with DEM L 87, the X-ray emission drops off, further suggesting interaction between the X-ray–emitting gas of N105 and DEM L 87.

3.7. *N144* (*DEM L 199*)

N144, encompassing the OB association LH 58, is a nebular region near the western rim of the supergiant shell LMC 3. A 120 pc × 75 pc ionized gas shell is visible in the Hα image (see Fig. 1*g*). The morphology of N144 is a roughly circular complex made up of many blister-like bubbles surrounding a central shell structure. The central shell has the brightest Hα emission of the nebula on its northern side. Diffuse X-ray emission is weakly detected toward several of the bubble regions, including the central bubble.

The X-ray emission is generally coincident with N144, and the strongest X-ray emission is toward the central shell seen in the Hα image. This indicates that the X-ray emission is likely to originate from the hot gas in the superbubble interior. There are two peaks in the X-ray emission from the central shell. These peaks generally coincide with the Wolf-Rayet stars Br 34 and Br 32, also cataloged as Sk −68°82 and Sk −68°80, indicating probable sources for the peaks in the diffuse X-ray emission (T. C. Hail, B. C. Dunne, & Y.-H. Chu 2001, in preparation). The X-ray emission extends beyond the Hα-emitting shell of the central bubble to the northeast and southwest. Each of these wings from the central concentration has its own weaker concentration of X-ray emission. This suggests that multiple-bubble structures in the N144 region have interior hot diffuse gas. The southwest wing of the X-ray emission shows further extension beyond the Hα shell of N144. This may indicate a breakout of the hot gas interior to N144 into a lower density region.

3.8. *N154* (*DEM L 246*)

N154 is a nebular complex to the south of the 30 Doradus region. The superbubble encompasses the OB associations LH 81 and LH 87. The 180 pc × 120 pc Hα shell of the superbubble is an angular, almost rhomboid shape, with the strongest Hα emission coming from the northeast and southwest sides. Diffuse X-ray emission is detected toward N154 (see Fig. 1*h*). A bright X-ray source to the southwest of N154 has been identified as SNR 0534−699 (Mathewson et al. 1983; Williams et al. 1999).

The diffuse X-ray emission toward N154 is centrally bright, and the morphology of the emission is that of an ellipsoid running southwest to northeast, similar to the structure and size of the Hα emission. It is reasonable therefore to assume that the diffuse X-ray emission arises from hot gas in the interior of the superbubble N154. There is significant X-ray emission trailing from N154 toward the northeast. Because of the strong X-ray background emission and number of X-ray sources near the 30 Doradus complex, it is difficult to determine whether this emission trail is a breakout region of hot X-ray–emitting gas from N154 or a blending of X-ray emission from N154 with emission from neighboring regions.

3.9. *N158* (*DEM L 269*)

N158 is a complex nebular structure to the south of 30 Doradus. The complex encompasses the OB associations LH 101 and LH 104. The superbubble is located on the northern part of the N158 complex and has a well-defined, 100 pc × 90 pc shell in the Hα. Diffuse X-ray emission is detected toward N158 (see Fig. 1*i*). Two strong X-ray sources are detected to the north and west of N158 as well. The source north of N158 appears to coincide with the known SNR and pulsar PSR B0540−69.3 (Mathewson et al. 1983; Bica et al. 1999), and the position of the source west of N158 is consistent with the *Einstein* X-ray source 0538.5−6925, a foreground Galactic star (Cowley et al. 1997).

The diffuse X-ray emission toward N158 appears to be coincident with the superbubble. Although the X-ray emission is not confined by the observed Hα shell, the morphology of the X-ray emission suggests that the emission is

[3] It should be noted here that the label "N103B" is often erroneously used to refer to the supernova remnant 0509−68.7. We are using N103B to refer to the Hα structure as originally identified by Henize (1956).

associated with N158, but that several breakout regions have formed along the shell where hot X-ray–emitting gas is escaping the interior of the superbubble. It must be cautioned, however, that the X-ray morphology of this region is exceedingly complex.

3.10. *N160 (DEM L 284)*

The nebular complex N160 is located on the southern side of the 30 Doradus region. The superbubble in N160 dominates the morphology of the complex. The superbubble is 180 pc × 150 pc in size and encompasses the OB association LH 103. The Hα morphology is roughly circular, with an apparent blowout region on the northeast edge (Points et al. 1999). The Hα emission is strongest on the southern edge of the superbubble, closest to LH 103. Diffuse X-ray emission is detected toward the superbubble (see Fig. 1*j*). Additionally, there is a pair of strong X-ray sources south of N160. These sources have been identified: the brighter source is the X-ray binary LMC X-1 and the dimmer source is SNR 0540−697 (Chu et al. 1997; Williams et al. 2000).

The diffuse X-ray emission detected toward the superbubble in N160 is concentrated near LH 103. Little significant emission is detected from the remainder of the superbubble. This suggests that the stars and/or supernovae in LH 103 are producing hot X-ray–emitting gas. The gas interior to the superbubble may be too hot to be detected in the PSPC energy bandpass, or the majority of the hot gas may simply have already escaped.

3.11. *N206 (DEM L 221)*

N206 (also cataloged as DEM L 221) is a nebular complex encompassing the OB associations LH 66 and LH 69. N206 contains both a superbubble and a smaller supernova remnant, SNR 532−710 (Mathewson et al. 1983; Williams et al. 1999). The 30 pc × 30 pc remnant is located on the eastern side of the nebular complex and has a faint circular Hα shell. The superbubble has a larger circular shell, 110 pc × 110 pc, with the brightest Hα emission coming from the eastern and southern sides of the bubble. Diffuse X-ray emission is detected toward both the remnant and the superbubble (see Fig. 1*k*). The diffuse X-ray emission detected toward the supernova remnant has been previously explored by Williams et al. (1999).

The diffuse X-ray emission toward the superbubble of N206 appears to have a several enhancements, possibly in a limb-brightened ring. The emission coincides with a region of the superbubble that is not bright in Hα, but the diffuse X-ray emission appears confined by faint Hα structures on the western side of the superbubble. Therefore, it is reasonable to conclude that the X-ray emission is produced by hot gas interior to the superbubble.

One of the enhancements of the diffuse X-ray emission coincides with the Wolf-Rayet star Br 44. The X-ray emission from this enhancement in the superbubble may therefore have a stellar source rather than a diffuse one. The emission from this enhancement has therefore been excluded from the thermal plasma model fit of the superbubble in N206.

3.12. *30 Dor C (DEM L 263)*

30 Dor C is a superbubble located in the southwestern region of the 30 Doradus complex. The superbubble encompasses the OB association LH 90. The Hα emission shows a strong shell structure, 100 pc × 90 pc. Diffuse X-ray emission is detected toward the superbubble (see Fig. 1*l*).

The X-ray emission detected toward 30 Dor C is limb-brightened and appears confined within the Hα shell. It is therefore reasonable to conclude that the X-ray emission arises from within the superbubble. The limb-brightened shell is well defined all around the superbubble except on the southwest, where the X-ray emission is near the background levels.

The absorption column density toward 30 Dor C is known to change dramatically across the face of the superbubble (J. Osterberg 1997, private communication). We have therefore divided 30 Dor C into two parts, east and west, to account for the change in absorption column density in our spectral fits. Unfortunately, the LMC $N_{\rm H\,I}$ maps from Rohlfs et al. (1984) do not have the spatial resolution to detect this change, so we must still use a single value in our fixed $N_{\rm H}$ fits of 30 Dor C.

4. DISCUSSION

4.1. *Distribution of X-Ray Luminosities*

Based on the spectral fits performed for each superbubble, we have computed X-ray luminosities. We have used these luminosities to investigate the superbubble luminosity function. In Figure 4, we present the X-ray luminosity function for the superbubbles in our data set. We have plotted the luminosities as determined by both the best-fit $N_{\rm H}$ model fits and the fixed $N_{\rm H}$ model fits. The best-fit $N_{\rm H}$ luminosity function illustrates that most of the superbubbles in our sample have X-ray luminosity around

TABLE 5

SUPERBUBBLE EMISSION MEASURES AND PRESSURE-DRIVEN MODEL X-RAY LUMINOSITIES

Object	Mean Emission Measure (cm^{-6} pc)	Size (pc × pc)	Expansion Velocity (km s^{-1})	$\log (L_X)_{\rm Model}$ (ergs s^{-1})	$\log (L_X)_{\rm Best\ Fit}$ (ergs s^{-1})	$\log (L_X)_{\rm Fixed}$ (ergs s^{-1})
N11 shell 1	~750	150 × 100	45	34.8	37.17	35.96
N44	~3000	100 × 75	40	35.1	35.73	36.36
N51 DEM L 192.....	~1750	135 × 120	20–50	34.8	35.18	35.82
N51 DEM L 205.....	~1200	65 × 50	45–70	35.1	34.86	35.37
N57	~1500	135 × 105	~45	35.0	35.32	35.91
N103B.....	~1000	120 × 120	20	34.2	34.85	35.02
N144	~1500	120 × 75	20–30	34.5	34.74	35.12
N158	~2000	120 × 100	~45	35.0	35.85	36.66
N160	~1250	180 × 150	$\lesssim$20	34.3	35.80	36.07
N206	~1500	90 × 90	~30	34.6	35.09	35.80
30 Dor C.....	~2000	100 × 90	~45	35.0	36.00	36.06

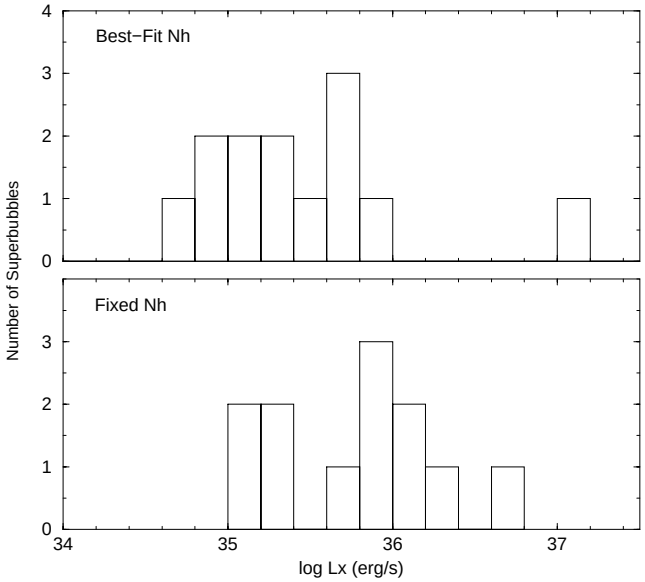

FIG. 4.—Superbubble X-ray luminosity distribution, showing X-ray luminosity plotted on a logarithmic scale. The 0.2 bin size was used.

10^{35}–10^{36} ergs s^{-1}. A single high-end outlier at more than 10^{37} ergs s^{-1} is also shown; this outlier is N11 shell 1. The fixed N_H luminosity distribution favors higher X-ray luminosities rather than the best-fit N_H luminosity distribution, as well as a broader range in luminosities (excepting the outlier on the best-fit N_H luminosity function).

4.2. *Pressure-driven Models*

To compare the X-ray luminosities of the superbubbles derived from observation with the pressure-driven bubble models of Weaver et al. (1977) for the LMC superbubbles, we have followed the procedure described in Paper I and corrected in Paper III. Assuming that the shell thickness is small compared to the radius of the bubble, that the electron temperature in the shell is $T_e \simeq 10^4$ K, and that the mean atomic mass of the ambient medium $\mu_a = (14/11)m_H$, we can use equations (7)–(10) from Paper III to derive the X-ray luminosity:

$$L_X \simeq 6.7 \times 10^{29} \mathrm{EM}^{5/7} \xi I R_{pc}^{12/7} v_{exp}^{1/7} \text{ erg s}^{-1} , \quad (1)$$

where ξ is the metallicity, assumed to be 0.3, I is a dimensionless function of the temperatures interior to the superbubble, which has a value ~ 2, EM is the emission measure of the 10^4 K shell gas in cm^{-6} pc, R_{pc} is the radius of the superbubble in parsecs, and v_{exp} is the superbubble expansion velocity in kilometers per second. The dimensions and expansion velocities of the superbubbles are given in Table 1. Unfortunately, we do not have expansion velocities for all the superbubbles. The emission measure was determined from the continuum-subtracted Hα image derived from the PDS scans of the Curtis Schmidt plates of Kennicutt & Hodge (1986). The emission measures and theoretical X-ray luminosities are presented in Table 5. Of course, the emission measure can vary greatly around the Hα shell, so we have taken a rough mean for each superbubble. The predicted X-ray luminosities range from $10^{34.3}$ to $10^{35.1}$ ergs s^{-1}. These luminosities range from ~ 3 to ~ 50 times lower than the X-ray luminosities determined from the PSPC data with the fixed N_H fits. This suggests that the majority of the X-rays are produced by mechanisms different than those described in the pressure-driven bubble model, confirming that the superbubbles in our sample are X-ray–bright.

4.3. *X-Ray Luminosity Correlations*

We have also compared the superbubble volume, Hα luminosity, expansion velocity, and bright star count with the X-ray luminosity, for both the best-fit and fixed N_H model fits (see Figs. 5, 6, 7, and 8). The superbubble volumes were determined from the sizes of the Hα shell (see Table 1),

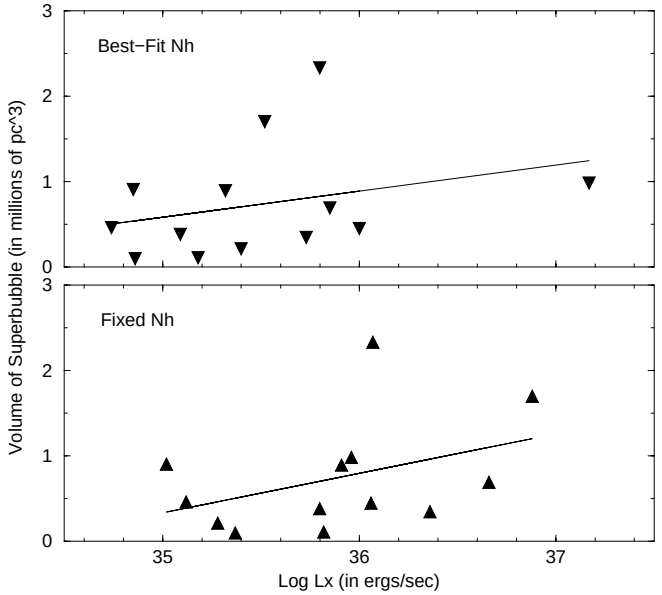

FIG. 5.—Superbubble X-ray luminosity vs. volume for the best-fit N_H X-ray spectral fits (*top*) and fixed N_H X-ray spectral fits (*bottom*). Luminosity is plotted on a logarithmic scale. The volumes are based on Hα morphology. A linear trend line is plotted for each graph.

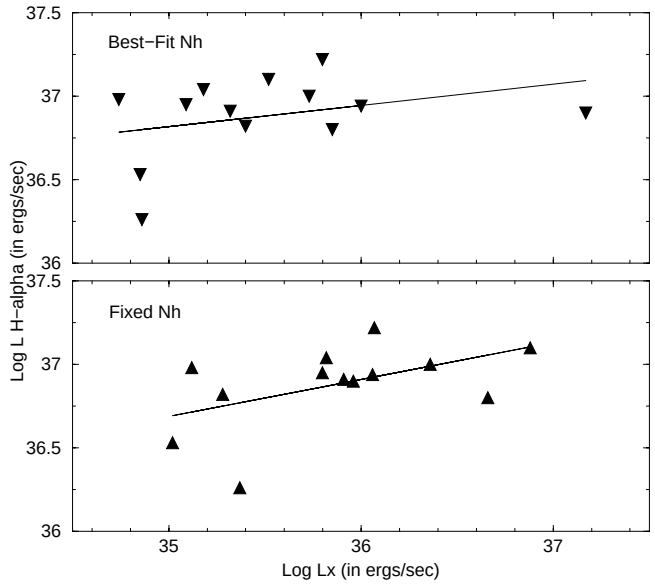

FIG. 6.—Superbubble X-ray luminosity vs. Hα luminosity for the best-fit N_H X-ray spectral fits (*top*) and fixed N_H X-ray spectral fits (*bottom*). Both luminosities are plotted on a logarithmic scale. A linear trend line is plotted for each graph.

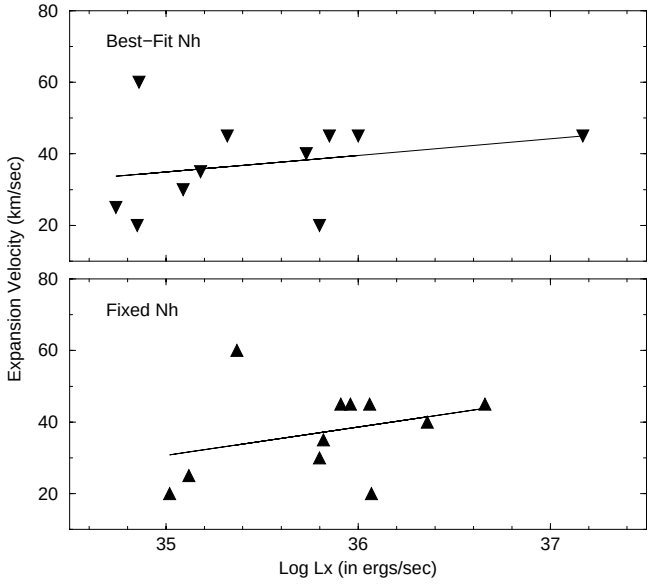

FIG. 7.—Superbubble X-ray luminosity vs. Hα expansion velocity for the best-fit N_H X-ray spectral fits (*top*) and fixed N_H X-ray spectral fits (*bottom*). Luminosity is plotted on a logarithmic scale. A linear trend line is plotted for each graph.

assuming an ellipsoidal shape. The expansion velocities and Hα luminosities are also given in Table 1. The bright star counts are based on the OB association star counts in Lucke & Hodge (1970); again, Table 1 lists the OB associations encompassed by each superbubble. Although the scatter level of these plots is obviously high, we have attempted to fit each plot with a linear trend line to test for correlations between X-ray luminosity and other superbubble properties. The correlation coefficients of the trends are detailed in Table 6. Positive correlations are found between X-ray luminosity and each of the other properties. The correlations are moderate for the X-ray

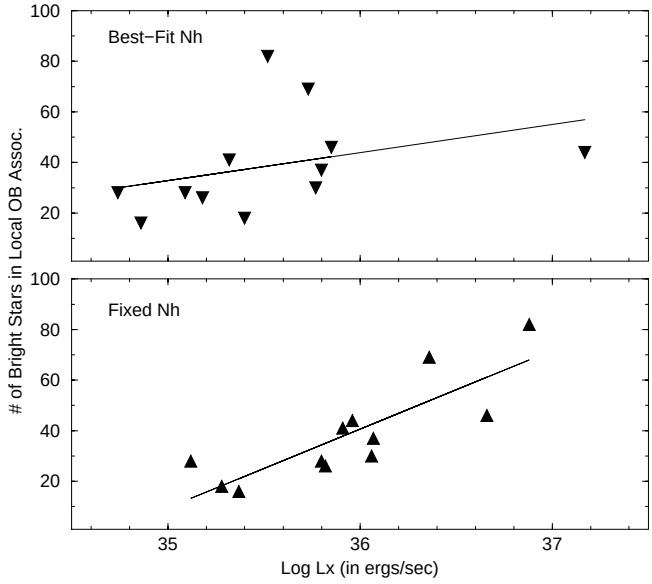

FIG. 8.—Superbubble X-ray luminosity vs. bright star count for the best-fit N_H X-ray spectral fits (*top*) and fixed N_H X-ray spectral fits (*bottom*). Luminosity is plotted on a logarithmic scale. Bright star counts are based on star counts in local OB associations (Lucke & Hodge 1970).

TABLE 6

CORRELATION COEFFICIENTS

	CORRELATION COEFFICIENTS	
PLOT L_X VS.	Best-Fit N_H	Fixed N_H
Superbubble volume.....	0.30	0.40
Hα luminosity	0.33	0.51
Expansion velocity	0.26	0.31
Bright star count.....	0.35	0.83

luminosities as determined by the best-fit N_H model fits and are generally stronger for the X-ray luminosities as determined by the fixed N_H model fits. The strongest correlation is between fixed N_H X-ray luminosity and bright star count. It must be considered, however, that the correlation between X-ray luminosity and superbubble volume may be due to a surface brightness selection effect.

The correlations demonstrate that the X-ray luminosity of a superbubble is affected by the richness and age of the OB associations within its shell walls. The bright star count of a superbubble is obviously directly related to the richness of its OB associations. Also, OB association richness provides stellar winds to power the expansion and thereby increase the expansion velocity of the superbubble. The Hα luminosity of a superbubble is positively affected by the richness of OB association, as more stars provide more ionizing flux, and negatively affected by age, as the powerfully ionizing early-type stars exhaust themselves. The X-ray luminosity–OB association richness relationship has already been demonstrated; however, the X-ray luminosity can increase with the age of a superbubble. As demonstrated by Paper I and Wang & Helfand (1991), the X-ray luminosity of a superbubble can be enhanced by SNRs. Thus, a superbubble that has already had several bright stars become supernovae can be brighter in X-rays than a superbubble with much younger OB associations. We would therefore expect the correlation between X-ray luminosity and Hα luminosity to be weaker than the correlation between X-ray luminosity and bright star count, which it is for the fixed N_H model fits.

4.4. *Stellar Sources and Breakout Regions*

We have described the X-ray morphology for each superbubble and compared those morphologies to the Hα morphologies and known stellar sources of each superbubble. We have found that in a significant fraction of the superbubbles, peaks in the X-ray emission coincide with known stellar sources, such as Wolf-Rayet stars. High-resolution observations are needed to determine whether the X-ray peaks are caused by stellar emission or stellar wind interactions with the superbubble interior gas. In addition, nearly half the superbubbles show some evidence of breakout regions in their X-ray morphologies, where hot gas appears to be leaking from the superbubble interior into the surrounding regions. Again, further studies of the diffuse X-ray gas are needed to confirm whether these regions are true breakout regions.

5. SUMMARY

We have presented *ROSAT* observations of thirteen LMC superbubbles. Eleven of these observations had not been reported previously. In each of these superbubbles, diffuse X-ray emission brighter than that theoretically

expected for a wind-blown bubble was detected. Based on the previous findings in Paper I and Wang & Helfand (1991), it is reasonable to conclude that the X-ray emission from the superbubbles has been enhanced by interactions between the superbubble shell and interior SNRs. We have also found significant positive correlations between the X-ray luminosity of a superbubble and its Hα luminosity, expansion velocity, and OB star count. Further, we have found that a large fraction of the superbubbles in the sample show evidence of breakout regions. Paper IV demonstrated that breakout regions can significantly affect the evolution of a superbubble, draining energy and pressure that would otherwise go into expansion. We also suggest that because these breakout regions appear so frequently the superbubbles may be a significant source of hot gas for the interstellar medium.

We would like to thank Robert Gruendl for his useful communications in preparing this paper. This research has made use of data obtained through the High Energy Astrophysics Science Archive Research Center Online Service, provided by the NASA/Goddard Space Flight Center. This research was made possible by ADP grants NAG 5-7003 and NAG 5-8003.

REFERENCES

Arabadjis, J. S., & Bregman, J. N. 1999, ApJ, 510, 806
Bica, E. L. D., Schmitt, H. R., Dutra, C. M., & Oliveira, H. L. 1999, AJ, 117, 238
Breysacher, J. 1981, A&AS, 43, 203
Chu, Y.-H., Chang, H.-W., Su, Y.-L., & Mac Low, M.-M. 1995, ApJ, 450, 157 (Paper III)
Chu, Y.-H., Kennicutt, R. C., Snowden, S. L., Smith, R. C., Williams, R. M., & Bomans, D. J. 1997, PASP, 109, 554
Chu, Y.-H., Kim, S., Points, S. D., Petre, R., & Snowden, S. L. 2000, AJ, 119, 2242
Chu, Y.-H., & Lasker, B. M. 1980, PASP, 92, 730
Chu, Y.-H., & Mac Low, M.-M. 1990, ApJ, 365, 510 (Paper I)
Chu, Y.-H., Mac Low, M.-M., Garcia-Segura, G., Wakker, B., & Kennicutt, R. C. 1993, ApJ, 414, 213 (Paper II)
Chu, Y.-H., Weis, K., & Garnett, D. R. 1999, AJ, 117, 1433
Cowley, A. P., Schmidtke, P. C., McGrath, T. K., Ponder, A. L., & Fertig, M. R. 1997, PASP, 109, 21
Davies, R. D., Elliott, K. H., & Meaburn J. 1976, MmRAS, 81, 89
Dickey, J. M., & Lockman, F. J. 1990, ARA&A, 28, 215
Feast, M. 1999, PASP, 111, 775
Georgelin, Y. M., Georgelin, Y. P., Laval, A., Monnet, G., & Rosado, M. 1983, A&AS, 54, 459
Henize, K. G. 1956, ApJS, 2, 315
Hodge, P. W., & Sexton, J. A. 1966, AJ, 71, 363
Kennicutt, R. C., & Hodge, P. W. 1986, ApJ, 306, 130
Lucke, P. B., & Hodge P. W. 1970, AJ, 75, 171
Mac Low, M.-M., Chang, T. H., Chu, Y.-H., Points, S. D., Smith, R. C., & Wakker, B. P. 1998, ApJ, 493, 260 (Paper V)
Magnier, E. A., Chu, Y.-H., Points, S. D., Hwang, U., & Smith, R. C. 1996, ApJ, 464, 829 (Paper IV)
Mathewson, D. S., Ford, V. L., Dopita, M. A., Tuohy, I. R., & Long, K. S. 1983, ApJS, 51, 345
Mathewson, D. S., Ford, V. L., Tuohy, I. R., Mills, B. Y., Turtle, A. J., & Helfand, D. J. 1985, ApJS, 58, 197
Meaburn, J., & Laspias, N. V. 1991, A&A, 245, 635
Morrison, R., & McCammon, D. 1983, ApJ, 270, 119
Pfefferman, E., et al. 1987, Proc. SPIE, 733, 519
Points, S. D., Chu, Y.-H., Kim, S., Smith, R. C., Snowden, S. L., Brandner, W., & Greundl, R. A. 1999, ApJ, 518, 298
Raymond, J. C., & Smith, B. W. 1977, ApJS, 35, 419
Rohlfs, K., Kreitschmann, J., Feitzinger, J. V., & Siegman, B. C. 1984, A&A, 137, 343
Rosado, M., Laval, A., Le Coarer, E., Georgelin, Y. P., Amram, P., Marcelin, M., Goldes, G., & Gach, J. L. 1996, A&A, 308, 588
ROSAT Mission Description. 1991 (NASA NRA 91-OSSA-25; Washington: GPO), Appendix F
Sanduleak, N. 1969, Contrib. Cerro Tololo Inter-American Obs., 89
Wang, Q., & Helfand, D. J. 1991, ApJ, 373, 497
Weaver, R., McCray, R., Castor, J., Shapiro, P., & Moore, R. 1977, ApJ, 218, 377
Williams, R. M., Chu, Y.-H., Dickel, J. R., Petre, R., Smith, R. C., & Tavarez, M. 1999, ApJS, 123, 467
Williams, R. M., Petre, R., Chu, Y.-H., & Chen, C. H. R. 2000, ApJ, 536, L27